Anisotropy of the spin-orbit coupling driven by a magnetic field in InAs nanowires

Paweł Wójcik [1,*] Andrea Bertoni [2,†] and Guido Goldoni [3,2,‡]

[1]*AGH University of Science and Technology, Faculty of Physics and Applied Computer Science, Al. Mickiewicza 30, 30-059 Krakow, Poland*
[2]*CNR-NANO S3, Istituto Nanoscienze, Via Campi 213/a, 41125 Modena, Italy*
[3]*Department of Physics, Informatics and Mathematics, University of Modena and Reggio Emilia, Via Campi 213/a, 41125 Modena, Italy*

(Received 23 November 2020; revised 25 January 2021; accepted 10 February 2021; published 23 February 2021)

We use the $\mathbf{k}\cdot\mathbf{p}$ theory and the envelope function approach to evaluate the Rashba spin-orbit coupling induced in a semiconductor nanowire by a magnetic field at different orientations, taking explicitly into account the prismatic symmetry of typical nanocrystals. We make the case for the strongly spin-orbit-coupled InAs semiconductor nanowires and investigate the anisotropy of the spin-orbit constant with respect to the field direction. At sufficiently high magnetic fields perpendicular to the nanowire, a sixfold anisotropy results from the interplay between the orbital effect of field and the prismatic symmetry of the nanowire. A backgate potential, breaking the native symmetry of the nanocrystal, couples to the magnetic field inducing a twofold anisotropy, with the spin-orbit coupling being maximized or minimized depending on the relative orientation of the two fields. We also investigate in-wire field configurations, which shows a trivial twofold symmetry when the field is rotated off the axis. However, isotropic spin-orbit coupling is restored if a sufficiently high gate potential is applied. Our calculations are shown to agree with recent experimental analysis of the vectorial character of the spin-orbit coupling for the same nanomaterial, providing a microscopic interpretation of the latter.

DOI: 10.1103/PhysRevB.103.085434

I. INTRODUCTION

The spin-orbit (SO) interaction, which couples the spin of electrons with their momentum, is the functioning principle of many spintronic applications, including spin transistor [1,2], spin filters [3–5], or spin-orbit qubits [6,7]. Recent investigations focus towards semiconductor nanowires (NWs) with strong SO interaction [8–16] as host materials for topological quantum computing based on Majorana zero energy modes [17–21]. These exotic quasiparticles form at the ends of a NW as a result of the interplay between the SO coupling, Zeeman spin splitting, and *s*-wave superconductivity induced in the NW by the proximity effect from a superconducting shell [22–24].

In general, a finite SO constant originates from the lack of the inversion symmetry. In semiconductors, this could either be an intrinsic feature of the crystallographic structure (Dresselhaus SO coupling [25]) or induced by the confinement potential (Rashba SO coupling [26,27]). In zincblende NWs grown along the [111] direction, the crystal inversion symmetry is preserved and the Dresselhaus term vanishes [10]. On the other hand, for spintronic applications the Rashba term has the essential advantage of being tunable by external fields, e.g., using external gates attached to the NW [28]. In general, external fields interplay with the overall NW geometry, which is typically prismatic, and the value of the SO constant depends on the position with respect to the underlying substrate, the details of the dielectric configuration, as well as on the compositional details of the NW which determine the electronic states [13,29]. For example, we have recently discussed the additional possibilities to engineer the SO constant in core-shell NWs with respect to homogeneous samples [12]. Since the SO constant depends, in general, on the symmetry and localization of the electronic states, a magnetic field may also induce a finite SO constant due to orbital effects.

Despite the number of experiments with measurements of the Rashba SO constant in semiconductor NWs [8–10], the study of its anisotropy with respect to the magnetic field orientation is limited. Recently, such a vectorial control was reported for InAs NWs which were suspended in order to eliminate the SO contribution originating from the substrate [30]. In Ref. [30] the authors tracked the nontrivial evolution of the weak antilocalization (WAL) signal and determined the SO length as a function of the magnetic field intensity and direction. Interestingly, they observed that the average SO coupling is isotropic with respect to the magnetic field orientation and does not reveal any hallmark of the prismatic symmetry. When applying a transverse electric field by a gate, however, a twofold anisotropy appears, with the maximal SO length when $\mathbf{B}$ is perpendicular to the electric field.

Motivated by the availability of such experiments, we use the 8×8 $\mathbf{k}\cdot\mathbf{p}$ method to analyze the dependence of the Rashba SO constant on the magnetic field intensity and orientation. The full vectorial character of the SO constant is taken into account by evaluating the SO coupling constants separately in different directions. While the magnetic field perpendicular to the NW axis is able to generate a finite SO constant which turns out to be isotropic at low intensity (below $\sim$1 T), for larger fields the SO constant shows a slight

*pawel.wojcik@fis.agh.edu.pl
†andrea.bertoni@nano.cnr.it
‡guido.goldoni@unimore.it

sixfold symmetry with respect to the field orientation, due to the interplay between the orbital effects of the field and the prismatic symmetry of the NW. A backgate potential couples to the magnetic field, which maximizes or minimizes the SO coupling depending on the relative orientation, leading to a twofold symmetry. We also investigate in-wire field configurations. The trivial twofold symmetry when the field is rotated in a plane which contains the axis is almost completely removed by a gate potential. Our results are discussed in light of recent experiments reported in Ref. [30].

The paper is organized as follows. In Sec. II the Rashba SO coefficients are derived from the 8×8 $\mathbf{k} \cdot \mathbf{p}$ model within the envelope function approximation, including the orbital effects which originate from the magnetic field. The effective Hamiltonian for the conduction electrons is derived in Sec. II A with details on the numerical method given in Sec. II B. Results of our calculations for homogeneous InAs NWs are reported in Sec. III, with a discussion of recent experiments. Section IV summaries our results.

II. THEORETICAL MODEL

We consider a homogeneous InAs NW with hexagonal cross section, grown along the [111] direction for which the Dresselhaus contribution to the SO interaction can be neglected [31]. The NW is subjected to the external magnetic field $\mathbf{B} = B\,(\cos\theta \sin\phi, \sin\theta \sin\phi, \cos\phi)$, with intensity B and the direction being defined by the angle ϕ formed with the NW axis along z and the angle θ formed with the x axis, which connects two corners of the NW in the x-y plane, see Fig. 1(a). We employ the gauge $\mathbf{A}(\mathbf{r}) = B\,(-y\cos\phi, 0, y\cos\theta\sin\phi - x\sin\theta\sin\phi)$. A backgate is directly attached to the bottom of the NW, along a facet, generating an electric field parallel to the NW section, in the x-y plane [10,13].

Below we use the 8×8 Kane model to derive the Rashba SO constants in terms of a realistic description of the quantum states in a magnetic field. This allows for quantitative predictions of SO coefficients as a function of the magnetic field and the gate voltage for different electron concentrations [12,13].

A. Effective SO Hamiltonian for conduction electrons

Our theoretical model is based on the 8×8 $\mathbf{k} \cdot \mathbf{p}$ Kane Hamiltonian within the envelope function approximation. We neglect here the spin Zeeman splitting, to focus on the dominating orbital effects, that is the distortion of the envelope function due to the field. It is straightforward to add the Zeeman splitting to the electron spin levels. The 8×8 Kane Hamiltonian reads [32]

$$H_{8\times 8} = \begin{pmatrix} H_c & H_{cv} \\ H_{cv}^\dagger & H_v \end{pmatrix}, \tag{1}$$

where H_c is the Hamiltonian of conduction electrons corresponding to the Γ_{6c} band, while H_v is the Hamiltonian of the valence bands, Γ_{8v}, Γ_{7v}

$$H_c = H_{\Gamma_6}\mathbf{1}_{2\times 2}, \tag{2}$$

$$H_v = H_{\Gamma_8}\mathbf{1}_{4\times 4} \oplus H_{\Gamma_7}\mathbf{1}_{2\times 2}. \tag{3}$$

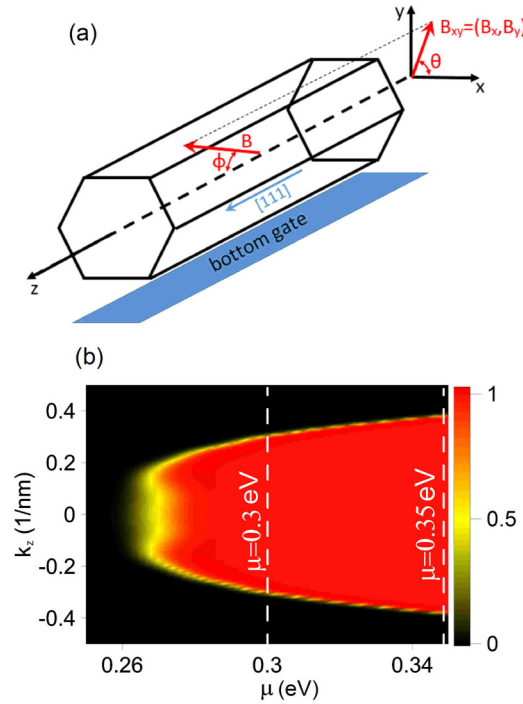

FIG. 1. (a) Schematics of a NW with a bottom gate. In our simulations, anisotropy is evaluated with a magnetic field $\mathbf{B}$ either perpendicular to the NW axis ($\phi = \pi/2$) and rotated with an azimuthal angle θ, or with $\theta = \pi/2$ and rotated in the y-z plane. (b) Occupation of the lowest subband as a function of the wave vector k_z at each chemical potential μ at $B = 4$ T. As μ increases, the occupation saturates to one at any k_z below the Fermi energy. Of course, in general several subbands are occupied. The nonparabolic dispersion is clearly appreciated, with the field inducing a seemingly Landau level dispersion. Two vertical dashed lines mark values of μ selected for the further analysis.

In the above expressions

$$H_{\Gamma_6} = -\frac{\mathbf{P}^2}{2m_0} + E_c + V(\mathbf{r}), \tag{4}$$

$$H_{\Gamma_8} = E_c + V(\mathbf{r}) - E_0, \tag{5}$$

$$H_{\Gamma_7} = E_c + V(\mathbf{r}) - E_0 - \Delta_0, \tag{6}$$

where $\mathbf{P} = \mathbf{p} - e\mathbf{A}(\mathbf{r})$, m_0 is the free electron mass, E_c is the conduction band edge, E_0 is the energy gap, Δ_0 is the split-off gap, and $V(\mathbf{r})$ is the potential energy. In our target systems, the potential $V(\mathbf{r})$ is the sum of the Hartree potential energy generated by the electron gas and the electrical potential induced by the bottom gate attached to NW, $V(\mathbf{r}) = V_H(\mathbf{r}) + V_g(\mathbf{r})$.

The off-diagonal matrix H_{cv} in (1) reads

$$H_{cv} = \frac{P_0}{\hbar}\begin{pmatrix} \frac{-P_+}{\sqrt{2}} & \sqrt{\frac{2}{3}}P_z & \frac{P_-}{\sqrt{6}} & 0 & \frac{-P_z}{\sqrt{3}} & \frac{-P_-}{\sqrt{3}} \\ 0 & \frac{-P_+}{\sqrt{6}} & \sqrt{\frac{2}{3}}P_z & \frac{P_-}{\sqrt{2}} & \frac{-P_+}{\sqrt{3}} & \frac{P_z}{\sqrt{3}} \end{pmatrix}, \tag{7}$$

where $P_\pm = P_x \pm iP_y$ and $P_0 = -i\hbar\langle S|\hat{p}_x|X\rangle/m_0$ is the conduction-to-valence band coupling with $|S\rangle$, $|X\rangle$ being the Bloch functions at the Γ point of Brillouin zone. Finally, the folding-down transformation [32]

$$\mathcal{H}(E) = H_c + H_{cv}(H_v - E)^{-1}H_{cv}^\dagger \tag{8}$$

reduces the 8×8 Hamiltonian (1) into the 2×2 effective Hamiltonian for the conduction band electrons.

The in-plane vector potential is introduced into the numerical model through the Peierls substitution [33]. Note that the field does not break translational invariance along the wire axis (the z direction). Therefore, assuming $\Psi_{n,k_z}(x,y,z) = [\Psi^{\uparrow}_{n,k_z}(x,y), \Psi^{\downarrow}_{n,k_z}(x,y)]^T e^{ik_z z}$ and expanding the on- and off-diagonal elements of the Hamiltonian (8) to second order, we obtain

$$\mathcal{H} = \left[\frac{\mathbf{P}_{2D}^2}{2m^*} + \frac{1}{2}m^*\omega_c^2\left[(y\cos\theta - x\sin\theta)\sin\phi - k_z l_B^2\right]^2 + E_c + V(x,y)\right]\mathbf{1}_{2\times 2} + (\alpha_x\sigma_x + \alpha_y\sigma_y)\frac{P_z}{\hbar}, \tag{9}$$

where $\mathbf{P}_{2D}^2 = P_x^2 + P_y^2 = (p_x + By\cos\phi)^2 + p_y^2$, $\omega_c = eB/m^*$, $l_B = \sqrt{\hbar/eB}$ is the magnetic length, σ_i are the Pauli matrices, m^* is the effective mass

$$\frac{1}{m^*} = \frac{1}{m_0} + \frac{2P_0^2}{3\hbar^2}\left(\frac{2}{E_g} + \frac{1}{E_g + \Delta_0}\right), \tag{10}$$

and α_x, α_y are the SO coefficients given by

$$\alpha_x(x,y) \approx \frac{P_0^2}{3}\left(\frac{1}{(E_0+\Delta_0)^2} - \frac{1}{E_0^2}\right)\frac{\partial V(x,y)}{\partial y}, \tag{11}$$

$$\alpha_y(x,y) \approx \frac{P_0^2}{3}\left(\frac{1}{(E_0+\Delta_0)^2} - \frac{1}{E_0^2}\right)\frac{\partial V(x,y)}{\partial x}. \tag{12}$$

B. SO coupling constants calculations

Representing the Hamiltonian (9) in the basis of the in-plane envelope functions $\psi_{n,k_z}(x,y)$, calculated without SO coupling, i.e., the diagonal part of (9), the matrix elements of the SO term are given by

$$\alpha_i^{nm}(k_z) = \iint \psi_{n,k_z}(x,y)\alpha_i(x,y)\psi_{m,k_z}(x,y)dxdy. \tag{13}$$

These coefficients define intra- ($n = m$) and intersubband ($n \neq m$) SO constants whose magnetic field dependence is studied in Sec. III. Note that the α's coefficients depend both on the envelope functions and the gradient of the potential.

Calculations of the $\psi_{n,k_z}(x,y)$'s is performed by the standard self-consistent Schrödinger-Poisson approach which includes electron-electron interaction at the mean-field level. First, the in-plane envelope functions $\psi_{n,k_z}(x,y)$ are determined from the diagonal term of (9)

$$\left[\frac{\mathbf{P}_{2D}^2}{2m^*} + \frac{1}{2}m^*\omega_c^2\left[(y\cos\theta - x\sin\theta)\sin\phi - k_z l_B^2\right]^2 + E_c + V(x,y)\right]\psi_{n,k_z}(x,y) = E_{n,k_z}\psi_{n,k_z}(x,y). \tag{14}$$

In the presence of a magnetic field, the subbands are not parabolic and $\psi_{n,k_z}(x,y)$ is explicitly k_z dependent. An example of the nonparabolic dispersion is shown in Fig. 1(b). Therefore, Eq. (14) is solved at selected k_z on a uniform grid in $[-k_z^{\max}, k_z^{\max}]$, with $k_z^{\max}$ fairly above the Fermi wave vector. Then, the electron density is obtained by

$$n_e(x,y) = 2\sum_n \int_{-k_z^{\max}}^{k_z^{\max}} \frac{1}{2\pi}|\psi_{n,k_z}(x,y)|^2 f(E_{n,k} - \mu, T)dk_z, \tag{15}$$

where the factor 2 accounts for spin degeneracy, T is the temperature, μ is the chemical potential, and $f(E_{n,k} - \mu, T)$ is the Fermi-Dirac distribution given by

$$f(E_{n,k} - \mu, T) = \frac{1}{1 + \exp\left(\frac{E_{n,k_z} - \mu}{k_B T}\right)}. \tag{16}$$

Finally, for a given $n_e(x,y)$ we solve the Poisson equation

$$\nabla_{2D}^2 V(x,y) = -\frac{n_e(x,y)}{\epsilon_0 \epsilon}, \tag{17}$$

where ϵ is the dielectric constant.

Equations (14) and (17) are solved numerically on a triangular grid assuming Dirichlet boundary conditions. The symmetry of the discretization grid matching the symmetry of the hexagonal integration domain avoids numerical artifacts at the boundaries using smaller grid densities. The procedure of alternately solving Eqs. (14) and (17) is repeated until self-consistency is reached, which we consider to occur when the relative variation of the charge density between two consecutive iterations is lower than 0.001 at every point of the discretization domain. Then, the self-consistent potential energy profile $V(x,y)$ and the corresponding envelope functions $\psi_{n,k_z}(x,y)$ are used to determine the SO constants α_i^{nm} from Eq. (13). Further details concerning the self-consistent method for hexagonal NWs can be found in our previous papers [34,35].

Calculations have been carried out for the material parameters corresponding to InAs [36]: $E_0 = 0.42$ eV, $\Delta_0 = 0.38$ eV, $m^* = 0.0265$, $E_P = 2m_0P^2/\hbar^2 = 21.5$ eV, $\epsilon = 15.15$, $T = 4.2$ K, and for the NW width $W = 100$ nm (facet-to-facet). In our calculations we fix the chemical potential. Results will be reported in the following section for $\mu = 0.3$ eV and $\mu = 0.35$ eV, which are marked by vertical dashed lines in Fig. 1(b). For $B = 0$, these values correspond to the electron concentration $n_e = 4.8 \times 10^{16}$ cm^{-3} and $n_e = 1.36 \times 10^{17}$ cm^{-3}, respectively. Note, however, that an increasing perpendicular magnetic field progressively depletes the NW [37]. Therefore, in a transport experiment the chemical potential must be set to a sufficiently large value. In our calculations, the above two values of μ have been chosen sufficiently large as to provide an occupied ground state at the largest magnetic field intensity used here, $B = 4$ T [Fig. 1(b)]. For a given magnetic field, different values of μ correspond to different occupations, hence a different self-consistent potential and charge distribution within the section of the NW, which in turn affects the SO coupling.

III. RESULTS

We shall now discuss predictions of the SO constant as a function of the magnetic field intensity and direction. We shall put particular emphasis on the role of the field-induced orbital effects and the interplay with the gate potential, which also influences electronic states localization and symmetry. We

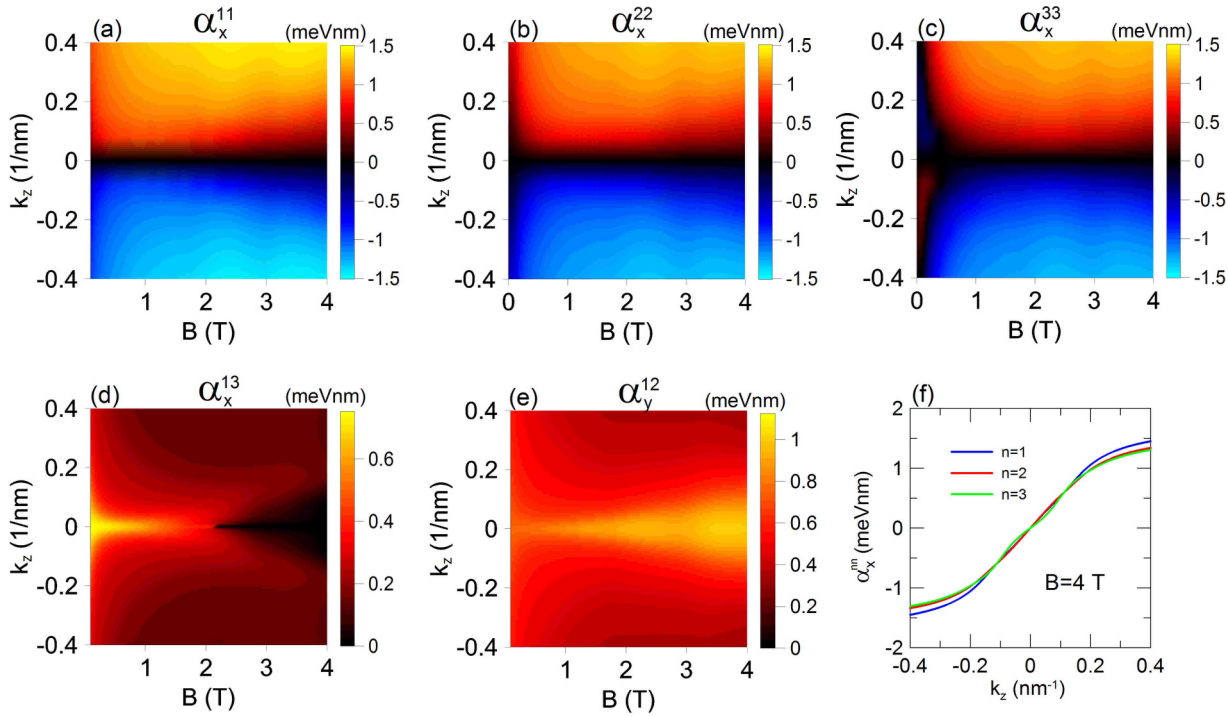

FIG. 2. (a)–(c) Intra- (α_i^{nn}, $n = 1, 2, 3$) and (d), (e) intersubband (α_i^{1m}) selected Rashba SO coupling constants as a function of the magnetic field B and the wave vector k_z. (f) $\alpha_i^{nn}(B, k_z)$ at $B = 4$ T for the three lowest states. Results are shown for $\mu = 0.3$ eV and a magnetic field perpendicular to the NW axis and along the corner-corner direction ($\phi = \pi/2, \theta = 0$).

conclude this section by a discussion of the recent experiment [30].

A. Perpendicular magnetic field with no backgate potential

We first show that a magnetic field perpendicular to the NW axis induces finite Rashba SO coefficients even in the absence of any transverse electric field ($V_g = 0$). In this case only the Hartree term V_H contributes to the self-consistent potential.

For $B = 0$ the self-consistent potential, having the same hexagonal symmetry of the confining potential of the NW, is symmetric with respect to the x and y directions. Hence, envelope functions have even or odd parity, leading to $\alpha_x^{nn} = \alpha_y^{nn} = 0$ for all electronic states, as implied by Eqs. (11)–(13).

Let us now consider a finite magnetic field, directed along, e.g, the x axis ($\phi = \pi/2, \theta = 0$). The field generates an effective parabolic potential along y, see Eq. (9), removing the symmetry of the Hamiltonian in this direction. This, in turn, induces a finite potential gradient and a k_z-dependent displacement of the envelope function, hence, finite diagonal SO couplings α_x^{nn} [see Eq. (11)], as shown in Figs. 2(a)–2(c) for selected subbands. For a constant Fermi energy, as assumed in our calculations, the number of occupied subbands changes with magnetic field. At $B = 1$ T, $N = 8$ subbands are occupied, while only $N = 3$ of them are populated at $B = 4$ T. The behavior of $\alpha_i^{nn}(k_z)$ $(i = x, y)$ for all three subbands is both qualitatively and quantitatively similar, especially for the high magnetic field, as presented in Fig. 2(f).

The maps of $\alpha_i^{nn}(B, k_z)$ in Figs. 2(d) and 2(e) report selected SO off-diagonal couplings between the ground state and the two lowest excited states. Other coefficients α_i^{1m} are four orders of magnitude lower than α_x^{11} and are not reported here. Note that the suppression of these off-diagonal matrix elements occurs only for a magnetic field along the corner-corner direction, $\theta = 0$. For an arbitrary direction of the magnetic field, no symmetry applies with respect to the specific x-y reference frame, and all off-diagonal SO constants have comparable values at $k_z = 0$.

The magnetic field dependence of α_i^{nn} can be traced to the envelope functions localization and ensuing self-consistent potential, as shown in Fig. 3. For $B = 0$ (not shown) the symmetry of the envelope functions naturally leads to $\alpha_i^{nn} = 0$ [13]. However, the field strongly changes the envelope function symmetry. The magnetic states of a NW have been thoroughly investigated in Ref. [37]. In short, at $k_z = 0$ these are localized by the field in the two corners along the field direction, where the vertical component of the field is the strongest, in seemingly dispersionless Landau levels [see also Fig. 1(b)]. Therefore, such states have the inversion symmetry and do not contribute to the SO coupling. At finite k_z the electron states are localized at one of the facets in dispersive states, which are the analog of the traveling edge states in a Hall bar. Accordingly, the SO constant α_x^{nn} is finite, it depends on k_z, and changes sign at $k_z = 0$, as shown in Figs. 2(a)–2(c). Note that $\pm k_z$ states have opposite localization along y. Therefore, regardless of the magnetic field intensity, the self-consistent potential, which is obtained by summing states up to the Fermi wave vector, has the inversion symmetry induced by the NW confinement, as shown in the right panels of Fig. 3.

For similar reasons, but with the opposite behavior due to symmetry, the intersubband SO couplings α_i^{1n} are largest at

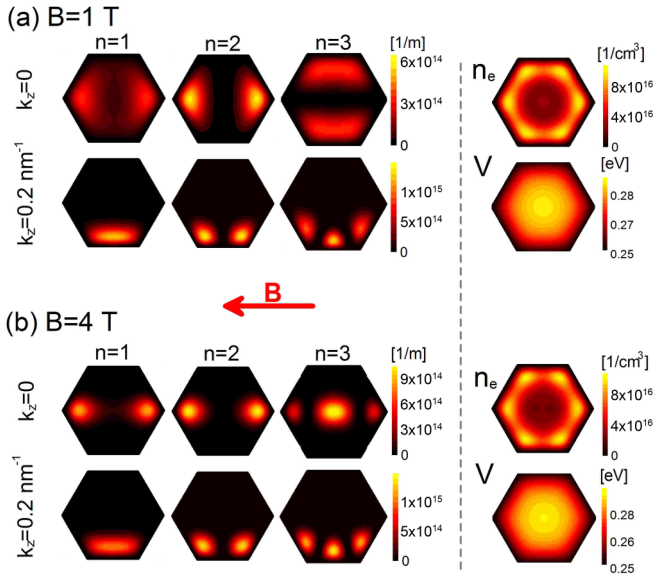

FIG. 3. Squared envelope functions of the three lowest magnetic subbands, at $k_z = 0$ and 0.2 nm^{-1}, with a transverse magnetic field (red arrow) at intensities (a) $B = 1$ T and (b) $B = 4$ T. Right panels show the electron density n_e and the self-consistent potential profile V at the corresponding field intensities.

$k_z = 0$. Its exact value strongly depends on the field intensity. Note that for the analyzed magnetic field direction the symmetry around the y axis is preserved, hence $\alpha_y^{nn} = 0$.

While a finite SO can be induced by a constant magnetic field due to the removal of the inversion symmetry, its magnitude also depends on the electric field in the NW, see Eqs. (11) and (12), which in turn depends on the electron concentration via the chemical potential μ. At sufficiently high electron density, the free charge moves to the corners of the NW to reduce the repulsive Coulomb energy [34]. The large gradient of the self-consistent potential where the envelope function is large generates SO constants α_i^{nn} which increase with μ. As an example, in Fig. 4(a) we show the calculated α_i^{11} as a function of the wave vector for $\mu = 0.30$ eV and $\mu = 0.35$ eV. Note that α_i^{11} increases rapidly with k_z but then saturates as the corresponding envelope functions are squeezed more and more to the NW edges.

In a transport experiment, electrons are injected in one of the subbands of the NW with a well defined Fermi wave vector, $k_{n,z}^F$, which is a function of the magnetic field intensity due to the field induced charge depletion. In Fig. 4(b) we show $\alpha_i^{nn}(V_g)$ at the Fermi wave vector $k_{n,z}^F$. The strong localization of the electron charge at opposite NW edges gives rise to a strong susceptibility of $\alpha_i^{nn}(V_g)$ around $B = 0$, analogously to what happens when a gate potential is switched on, as we discussed in Ref. [13]. On the other hand, α_i^{nn} saturates for high magnetic fields due to the orbital effect which squeezes the envelope functions to NW edges. Slight oscillations of $\alpha_x^{nn}(B)$ correspond to changes in the self-consistent potential due to depopulation of subsequent subbands when increasing field [see the black line in Fig. 4(b)].

We next analyze the anisotropy of the SO constant with respect to the transverse field direction. Indeed, as a finite α_i^{nn} originates from the confinement induced by the field, it is expected that the latter intertwines with the natural confinement of the electron charge at the NW edges, as discussed above. Therefore, we expect a sixfold anisotropy with respect to θ.

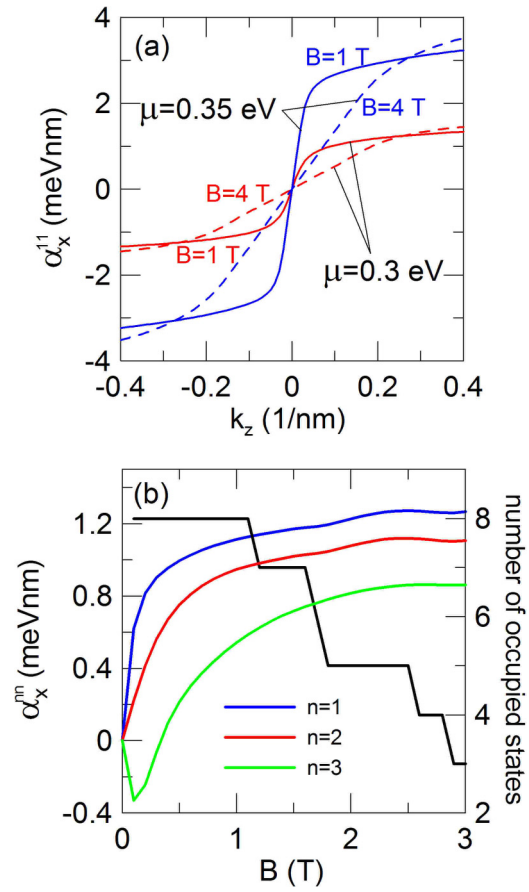

FIG. 4. (a) The intrasubband SO constant α_x^{11} as a function of k_z at $B = 1$ T and $B = 4$ T and at chemical potentials $\mu = 0.30$ eV and $\mu = 0.35$ eV. (b) The intrasubband SO constant $\alpha_x^{nn}(k_{n,z}^F)$, $n = 1, 2, 3$ (left axis) calculated at $k_{n,z}^F$ and number of occupied subbands (black line, right axis) as a function of the magnetic field intensity B.

The angular dependence of the intrasubband SO couplings is shown in Fig. 5 for the three lowest subbands and different magnetic field intensities. Note these subbands exhaust the occupied states at $B = 4$ T, but they are only a subset of the $N = 8$ occupied subbands at $B = 1$ T [see also Fig. 4(b)]. Subbands with $N > 3$ are not shown here, however, as they do not add information.

In Fig. 6 we show $\alpha^{nn} = \sqrt{(\alpha_x^{nn})^2 + (\alpha_y^{nn})^2}$ calculated for the ground state $n = 1$. The SO coupling α^{11} appears isotropic and unaffected by the magnetic field orientation. However, a very weak dependence on θ can be observed in the bottom subpanels which zoom in the k_z range marked by the dashed rectangular at the main graph. A similar weak sixfold anisotropy is shown by all the occupied states and corresponds to the hexagonal geometry of NW. It is due to the slight reshaping of the envelope functions which localize alternately on facets and corners as the magnetic field is rotated around the NW (see Fig. 7).

Interestingly, at $B = 4$ T the SO coupling shows a flower-like pattern around $k_z = 0$ for $n = 1, 2$, see Fig. 5(b), at low k_z.

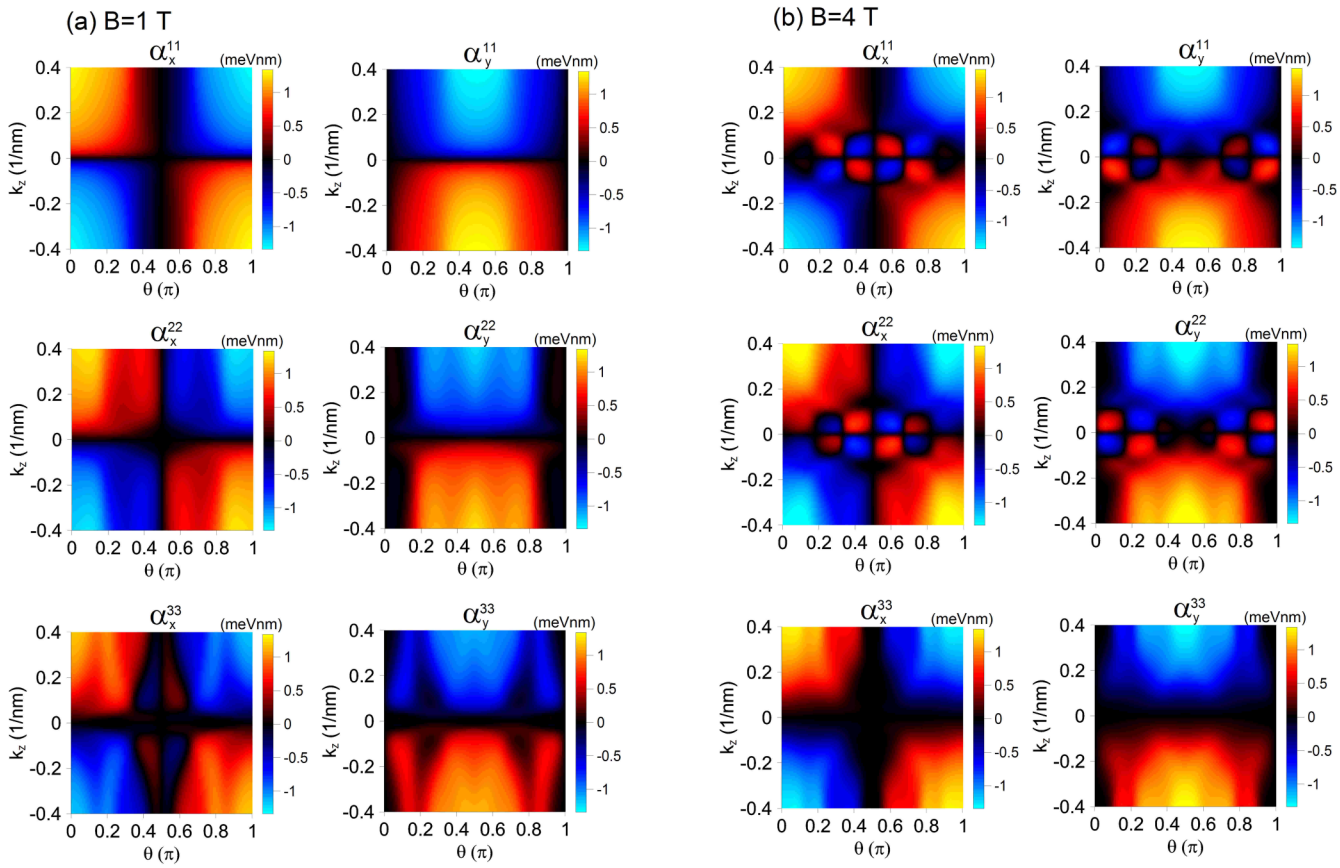

FIG. 5. Maps of α_x^{nn} and α_y^{nn} as a function of θ and wave vector k_z. Results are shown for $\mu = 0.30$ eV and magnetic fields (a) $B = 1$ T and (b) $B = 4$ T.

Indeed, when k_z is large, the parabolic well generated by the field strongly confines the charge near to the surface, similarly to edge states in a Hall bar. When squeezing is strong, the field orientation changes the localization of the wave function as presented in Fig. 7(b). Regardless of the field direction the envelope function remains localized near to the surface which results in a weak anisotropy of SOC.

At small k_z, instead, states are confined in the middle of the structure (similarly to Landau levels). There, the localization of the envelope function is only slightly affected by the field direction: At $\theta = 28^\circ$ (that is, along the shorter diagonal, large tunneling energy) a symmetric localization is stabilized, while at $\theta = 57^\circ$ (that is, near to the longer diagonals, small tunneling energy), a configuration of two strongly asymmetric lobes appears.

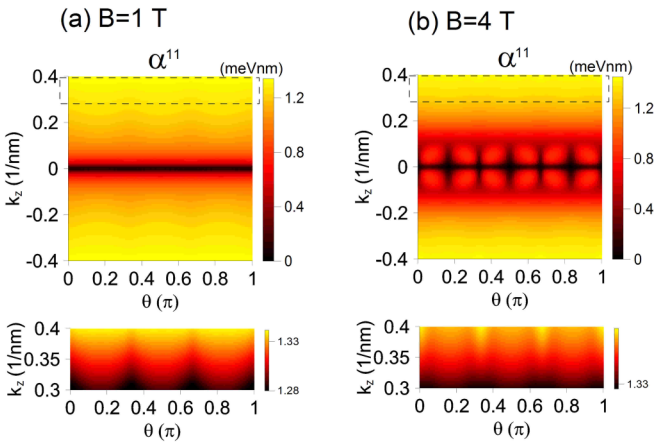

FIG. 6. Maps of α^{11} as a function of θ and wave vector k_z. Results are shown for $\mu = 0.30$ eV and magnetic fields (a) $B = 1$ T and (b) $B = 4$ T. Insets under the main panels zoom in the k_z range marked by dashed black rectangle of the corresponding panel.

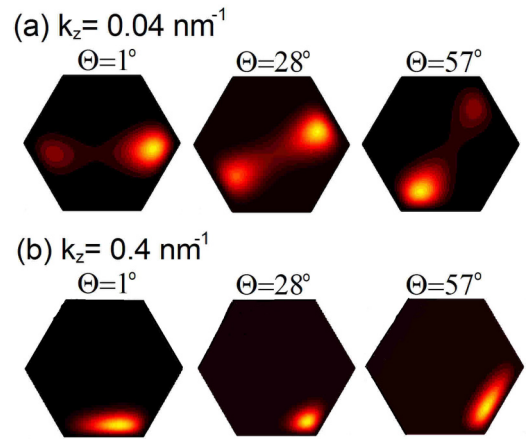

FIG. 7. Squared envelope function of the ground state at selected angles θ at $B = 4$ T. (a) $k_z = 0.04$ nm^{-1}, (b) $k_z = 0.4$ nm^{-1}.

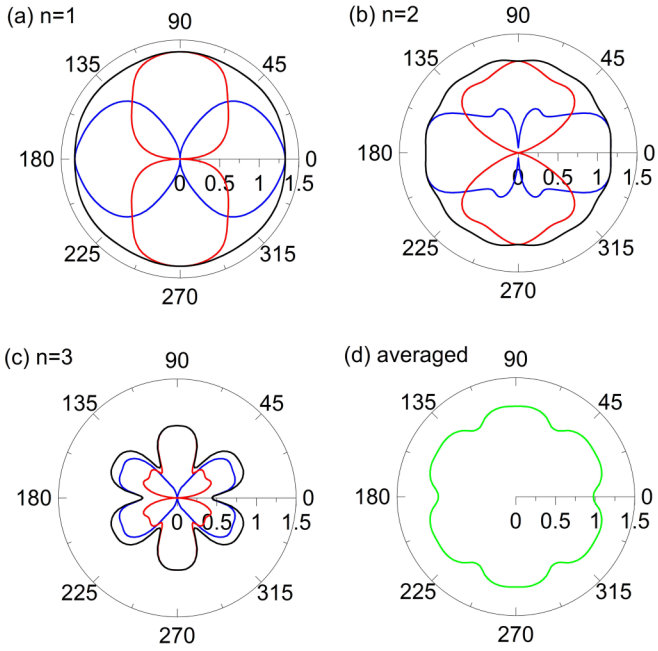

FIG. 8. (a)–(c) Angular dependence of the x (blue) and y (red) components of intrasubband SO coupling constant (in units of meV nm) at $k^F_{n,z}$ together with the modulus $\alpha^{nn} = \sqrt{(\alpha^{nn}_x)^2 + (\alpha^{nn}_y)^2}$ (black) for the three occupied states. Panel (d) presents the total SO coupling constant $\alpha_{\rm tot}$ averaged over all occupied states. Results for $B = 4$ T, $\mu = 0.3$ eV.

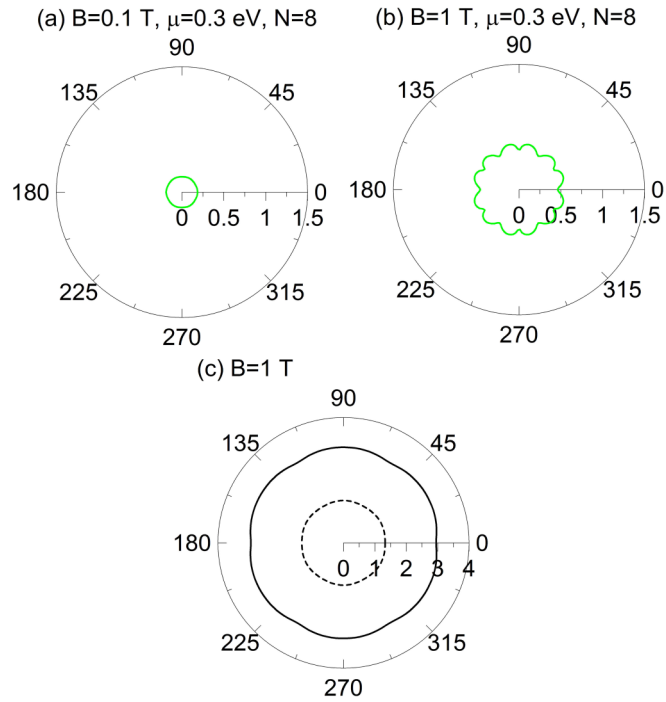

FIG. 9. The angular dependence of the total SO coupling constant (in units of meV nm) $\alpha_{\rm tot}$, averaged over all N occupied subbands at $k^F_{n,z}$. (a) $B = 0.1$ T, $\mu = 0.3$ eV ($N = 8$) and (b) $B = 1$ T, $\mu = 0.3$ eV ($N = 8$). (c) α^{11} at $\mu = 0.3$ eV (dashed line) and $\mu = 0.35$ eV (solid line).

In Figs. 8(a)–8(c) we report polar diagrams of the intrasubband SO constant calculated at the Fermi wave vector $k^F_{n,z}$ for all occupied states ($N = 3$) at $B = 4$ T. The x and y components and the modulus α^{nn} are shown separately. The value of SOC is the largest for the ground state, panel (a), which is almost isotropic. On the contrary, other electronic bands have a smaller value but a stronger anisotropy. The total SOC, $\alpha_{\rm tot} = (1/N)\sum_n \alpha^{nn}(k^F_{n,z})$, averaged over all occupied subbands, panel (d), to be compared with the observed value in the magnetotransport experiment, shows a slight sixfold anisotropy, with the smaller value along the corner-corner direction and the larger value along the facet-facet direction.

The total SOC for different B and μ is shown in Fig. 9. At the lowest magnetic field $B = 0.1$ T, panel (a), we do not observe any anisotropy. A slight sixfold anisotropy can be appreciated at $B = 1$ T, in panel (b). In this case a different behavior of the SOC as compared to that obtained at $B = 4$ T is due to the averaging over a larger number of subbands ($N = 8$), including higher excited states whose angular dependence is a combined effect of the orbital effects and the envelope function symmetry. Although the orbital effects for these higher excited states are suppressed due to low $k_{n,F}$, and therefore the contribution of them to the SOC is reduced, they cause visible ripples of SOC but still with the lowest SOC along the corner-corner line.

The observed sixfold anisotropy of SOC is actually expected. Due to external confinement and the self-consistent field arising from Coulomb interaction, the electron gas is strongly localized near the edges of NW for low B. A weak magnetic field cannot perturbate the symmetry of such strongly localized states. For higher magnetic field the Coulomb interaction weakens due to the magnetically induced charge depletion [see Fig. 4(b)]. Therefore a sufficiently strong magnetic field may squeeze the envelope functions to the surface in a way which depends on the relative orientation of the surface and the field. Note that the localization of the wave function at the surface is enhanced by the Coulomb repulsion at the high concentration regime. Indeed, as presented in Fig. 9(c), the sixfold anisotropy of α^{11} (for the ground state) is somewhat larger for higher μ.

Our results qualitatively agree with experimental evidence in Ref. [30] where the SO coupling was measured to be isotropic in a suspended hexagonal InAs NW. This negative result is expected in the low magnetic field used in the experiments ($B < 0.1$ T). Evaluating the field intensity at which anisotropy is exposed is a nontrivial issue. The reason is that increasing the field enhances the orbital effects on the charge density, which at zero field tends to be localized near to the surface, but it also depletes the NW from free charge, which makes the charge to delocalize, due to the small Coulomb repulsion, and less sensitive to the anisotropy of the NW.

B. Perpendicular magnetic field with a finite backgate potential

Next we consider the effect of a bottom gate attached to the NW (see Fig. 1). As in the previous section, the magnetic field is perpendicular to the NW axis. We first consider the $\theta = 0$ (corner-to-corner) direction, hence the two fields are orthogonal to each other.

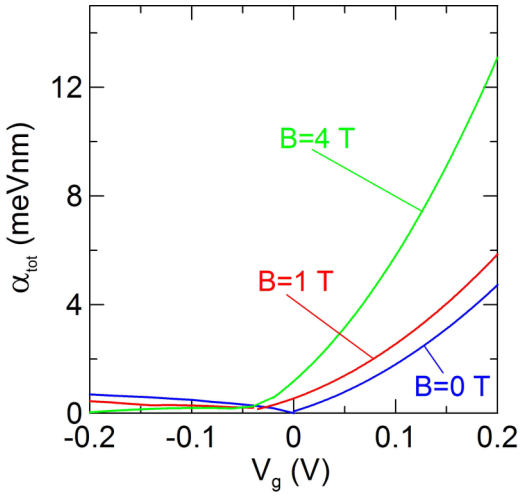

FIG. 10. The total intrasubband SO $\alpha_{\rm tot}$, as a function of V_g at selected magnetic fields $B = 0,\ 1,\ 4$ T directed in the $\theta = 0$ (corner-to-corner) direction. Results are shown for $\mu = 0.30$ eV.

The total intrasubband SO coupling $\alpha_{\rm tot}$ averaged over all occupied states at the Fermi wave vector $k^F_{n,z}$ is shown in Fig. 10 as a function of the backgate potential V_g at selected field intensities. For the present fields configuration the symmetry around the y axis is not broken, hence $\alpha^{nn}_y(V_g) = 0$. Figure 10 shows that $\alpha_{\rm tot}(V_g)$, which is finite due to the broken symmetry along x, increases with B for $V_g > 0$. $\alpha_{\rm tot}$ takes off at a threshold V_g which moves toward negative gate voltages with increasing magnetic field.

The strong asymmetry shown in Fig. 10 between positive and negative voltages is easily understood. For positive voltages the electron charge is pulled toward the gates, where the self-consistent field has the largest gradient. For negative voltages, instead, electrons are pulled far from the gate, where the potential is almost flat [13]. Note, however, the opposite effect of the magnetic field. Here, the electric and magnetic fields are orthogonal, $\theta = 0$. Therefore, for positive voltages both the gate potential and the magnetic field push electrons toward the bottom edge, hence the magnetic field reinforces the back gate effect, increasing the SO coupling. The opposite is true for $V_g < 0$; in this case, electric and magnetic field push the electrons on opposite sides, and the magnetic field weakens the SO coupling. Of course, the opposite situation takes place when the magnetic field is directed at $\theta = 180^\circ$. Therefore, for a fixed V_g, we expect a strong anisotropy with respect to the magnetic field orientation, as shown below.

Figure 11 shows the polar plot of $\alpha_{\rm tot}$ averaged over $k^F_{n,z}$ for $V_g = 0.1$ V together with α^{11}_i. In the absence of a magnetic field, the electronic charge is strongly localized by the electric field at the edge of the NW, near to the backgate. At a small magnetic field [$B = 0.1$ T in panel (a)], the orbital effects are negligible, and the SO coupling is isotropic. If we increase the magnetic field [panel (b)], however, $\alpha_{\rm tot}$ (as well as α^{11}_x) shows a twofold anisotropy, as expected from the interplay between the two fields. Note that at $\theta = 180^\circ$, the SO coupling of the ground state is nearly zero as the orbital effects localize the electron wave function near the upper facet (see the inset), overcoming the gate effect. There, the electric field is weak

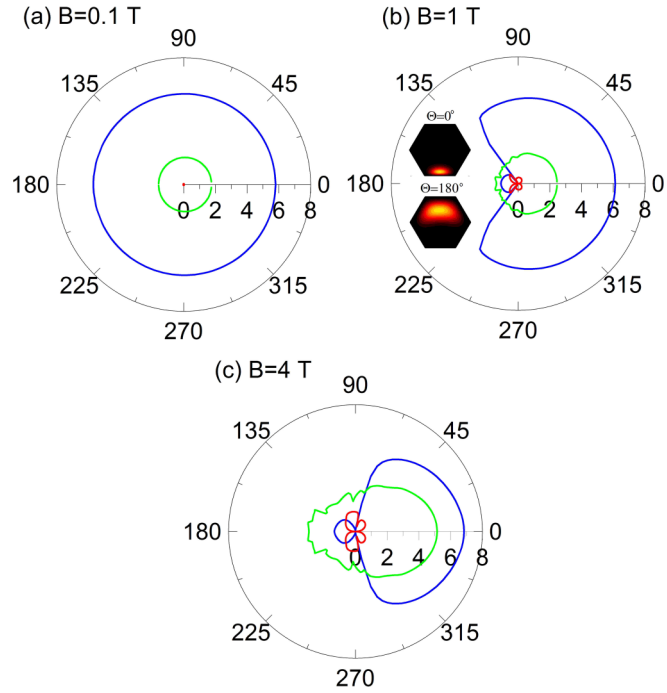

FIG. 11. The angular dependence of the x (blue) and y component (red) of the intrasubband SO constant (in units of meV nm) α^{11}_i calculated at the Fermi wave vector $k^F_{1,z}$ for the lowest subband and the total SO constant averaged over all occupied states at $k^F_{n,z}$ (green line). Insets in panel (b) show the squared envelope functions of the lowest subband at $k^F_{1,z}$ for the magnetic field with $\theta = 0$ and $\theta = 180^\circ$. Calculations are performed with $\mu = 0.30$ eV and $V_g = 0.1$ eV.

due to the distance from the gate, and the gradient is almost vanishing [13]. The nonzero value of $\alpha_{\rm tot}$ in this case results from the other states which contribute to the total SOC. Further increasing the field intensity B enhances the orbital effect enhancing the anisotropy due to suppressing α^{nn}_x in a wide angular range, as shown in panel (c) for the ground state.

A similar twofold anisotropy has been reported in Ref. [30] with a different gate configuration but with the same symmetry. We postpone the detailed analysis of this experiment to Sec. III D.

C. Axial magnetic field

We now consider the SO coupling constants under a magnetic field with a component along the NW axis. This is the relevant configuration in the context of Majorana states engineering, which requires the axially magnetic field and the SO interaction to create Majorana zero energy modes at the ends of a NW. The question concerning the relative relationship between the SO coupling and the magnetic field is still an open issue [29,33,38].

Figure 12 shows the calculated $\alpha_{\rm tot}(V_g)$ vs field intensity B with an axial field ($\phi = 0$). Clearly, the axial magnetic field affects the SO coupling to a slight extent up to $B = 16$ T. This is in agreement with previous calculations within the spin density functional formalism [39]. Indeed, in the axial field configuration, the inversion symmetry is not removed [see Eq. (9)], although the orbital effect is still visible in the

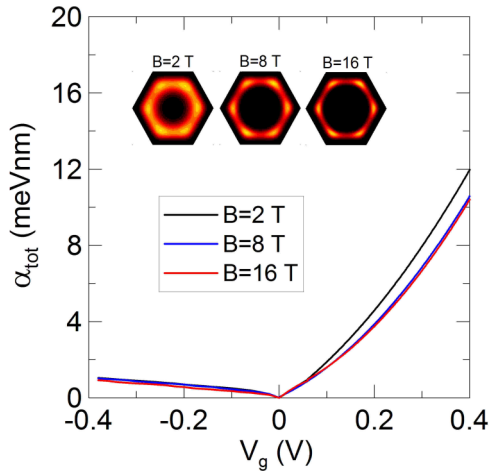

FIG. 12. The total intrasubband SO constant α_{tot} as a function of the gate voltage V_g for different axial magnetic fields. Inset: squared envelope functions of the lowest subband for different magnetic fields at $V_g = 0$.

inset of Fig. 12, where the envelope function is shown to localize further at the edges with the field. There is almost no field-induced depletion effect here, which is only due to the part of the orbital effect related to the field-induced quadratic terms in Eq. (9). Note the strong asymmetry with respect to the gate potential, which has the same explanation as the one in Fig. 10.

Next, we consider a magnetic field rotating in the y-z plane, see Fig. 13, which shows a twofold anisotropy. However, the anisotropy is almost removed by the gate potential, with the SO constant being only slightly larger for the axially magnetic field.

The behavior shown in Fig. 13 is easily traced to the wave function localization. At $V_g = 0$, SOC is trivially zero if the magnetic field is in the axial direction (inversion symmetry holds), while it is at maximum with the field in the orthogonal direction, $\phi = \pi/2$, as discussed in the previous paragraphs. If $V_g = 0.1$ V, instead, the wave function is localized near to the bottom edge, where the electric field is the largest, and the SO coupling is large as well. At $B = 1$ T the magnetic field

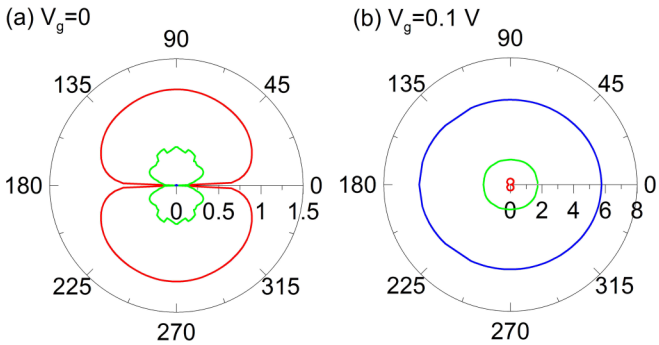

FIG. 13. Angular dependence of the x (blue) and y (red) component of the intrasubband SO (in units of meV nm) of the ground state α_i^{11} calculated at $k_{1,z}^F$ together with the total SOC α_{tot} (green). The magnetic field is rotated in the y-z plane. Results for $\mu = 0.30$ V, $B = 1$ T and (a) $V_g = 0$ and (b) $V_g = 0.1$ V.

changes the localization to a small extent, constantly keeping the wave function near the bottom gate. If the magnetic field is perpendicular to NW the orbital effects slightly squeeze the wave function to the side edges (either to the right or to the left corners) where the electric field is lower, slightly lowering the SO coupling. Hence, a small gate potential restores the y-z isotropy.

D. Comparison with experiment

In Ref. [30] the authors used magnetotransport experiments to determine the SO coupling in suspended InAs NWs. Using a vectorial magnet, the nontrivial evolution of weak antilocalization is tracked and the SO length is determined as a function of the magnetic field intensity and direction. This study shows no anisotropy related to the geometrical confinement in a low field regime. The isotropy of SO coupling is, however, removed in the presence of an external electric field induced by side gates. In this case, the SO coupling demonstrates a twofold periodic angular modulation when the magnetic field is rotated in both the y-z and x-y plane.

To simulate the experimental conditions, we consider a InAs NW attached to two side electrodes located 200 nm from the NW, see Fig. 14(a). Potentials applied to the gates generate an electric field which is assumed to change linearly in the region between the electrodes. All parameters are taken from the experiment. We assume $W = 100$ nm (facet-facet) and $n_e = 2 \times 10^{18}$ cm^{-3}, which for the considered NW geometry, gives $E_F = 0.935$ eV. In order to keep the electron density constant, the field is induced by applying an asymmetric potential $V_{SG1} = \alpha_g V_{SG2}$, where α_g is determined separately for each V_g, as to keep the density constant. We consider only the case with the magnetic field directed perpendicular to the NW and rotating in the x-y plane, with $B = 0.1$ T as used in the experiment.

The x and y components of the intrasubband SO coupling for the ground state α_i^{11} calculated at $V_g = 0$ is presented in Figs. 14(b) and 14(c). The rapid switch between the two components results from the Coulomb interaction. At the considered high electron concentrations the electron-electron repulsion localizes the charge in quasi-1D channels at the corners [34]. When the magnetic field rotates the localization of the ground state suddenly moves between the corners resulting in a steplike change between the x and y components which swap their intensities.

The total SO coupling constant averaged over all occupied states at $k_{n,F}^z$ is presented in panels (d) and (e) for two different gate voltages. The total SO coupling at $V_g = 0$, panel (d), is nearly isotropic exhibiting slight oscillations with the sixfold symmetry due to the prismatic symmetry of the NW which, in the considered high electron density regime, is more pronounced due to the strong localization of electrons at the six corners. Note that in Ref. [30] the authors reported full isotropic behavior of SOC at $V_g = 0$ without the oscillations. This inconsistency remains to be clarified. It may be the result of the specific extraction of the SO length used in Ref. [30] which includes the correction from the effective NW width. Alternatively, a low resolution of the magnetotransport measurement might not be able to capture small changes of SOC.

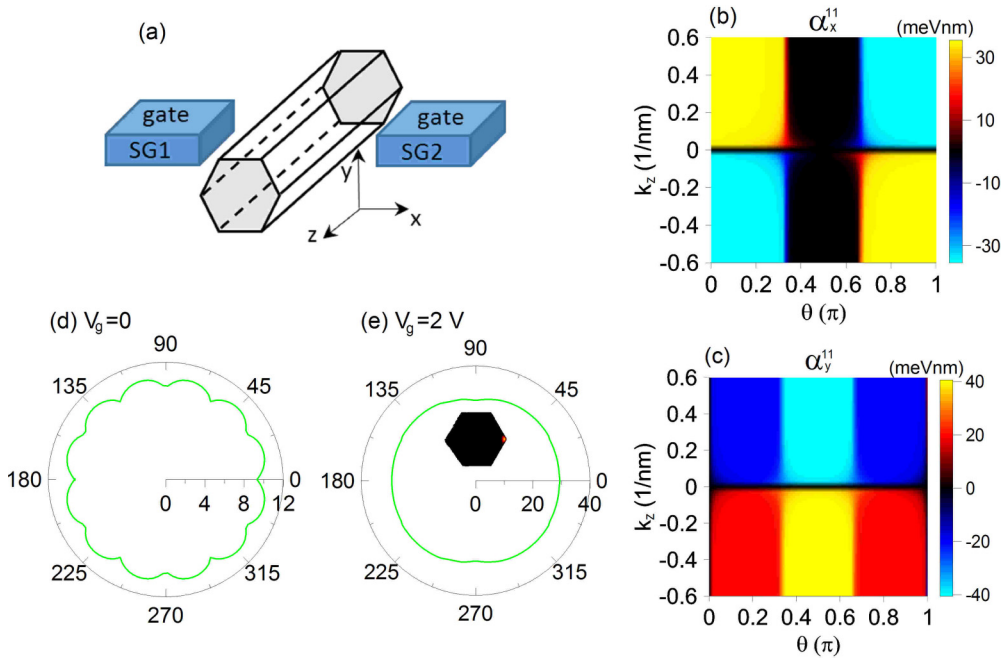

FIG. 14. (a) Schematic illustration of the experimental setup. (b), (c) The x and y component of the intrasubband SO coupling α_i^{11} as a function of the angle θ and the wave vector k_z. The magnetic field is rotated in the x-y plane. (d), (e) The angular dependence of the total SO constant α_{tot}. Results for $B = 0.1$ T and $\phi = \pi/2$.

Finally, we apply a potential $V_g = 2$ V, as in the experiments, to the side electrodes ($\alpha_g = 0.96$). In this configuration, the y component of SO coupling becomes dominant and is barely affected by the magnetic field orientation. For such a high gate potential the wave function of the ground state is strongly localized in the right corner [see the inset of Fig. 14(e)], and it is only slightly disturbed by the orbital effects originating from the weak magnetic field used in the experiment ($B = 0.1$ T). This results in the slight twofold anisotropy of SOC, shown in panel (e), similarly as reported in the experiment [30]. Note however that the experimental evidence shows a twofold anisotropy with respect to the magnetic field orientation in the y-z plane (although authors suggested its existence also in the x-y magnetic field rotation) and its intensity is much stronger.

Although we did not perform explicit calculations in this configuration for such a high electron density, which implies a very large number of subbands (∼100) and a correspondingly large numerical effort, results presented in Fig. 13 for a lower electron density and higher magnetic field agree with the experimental result and support the interpretation. Note however that at $V_g = 0$ and the axially directed magnetic field, the inversion symmetry around either the x and y axis is not broken, which results in $\alpha_{\text{tot}} = 0$ as presented in Fig. 13(a). This scenario is, however, not supported by the experimental data which exhibit nonzero SOC even for the axially magnetic field. This strongly suggests the presence in the samples of an intrinsic electric field of an unknown origin, which is a source of SO coupling whose distortion by the weak magnetic field used in the experiment ($B = 0.1$ T) is not possible, resulting in the isotropic SOC. An intrinsic electric field would also explain the absence of the SO coupling angular oscillations [as in Fig. 14(a)] and the slightly lower value of SOC from the calculations, $\alpha_{\text{tot}} \approx 10$ meV nm, as compared with the corresponding experimental value $\alpha_{\text{tot}}^{\text{exp}} \approx 15$ meV nm. Interestingly, it might also explain the observed unexplained phase shift in the magnetoconductance measurement (see Figs. 3(c) and 3(d) in Ref. [30]) in terms of the relative alignment between the magnetic field and the resultant electric field (sum of the noncollinear intrinsic and extrinsic electric field) which changes depending on the applied voltage.

IV. SUMMARY

Based on the $\mathbf{k} \cdot \mathbf{p}$ theory within the envelope function approximation, we have analyzed the orbital effects of a magnetic field on the Rashba SO coupling in InAs homogeneous semiconductor NWs. The full vectorial character of the SO constant has been studied under the magnetic field magnitude and orientation.

The Rashba SO interaction of conduction electrons in a NW is determined by the position and symmetry of the electron's wave function, which can be tuned by gate-induced electric fields as well as by the the orbital effects induced by a magnetic field. Specifically, when we apply the magnetic field perpendicular to NW, the inversion symmetry of the envelope functions is broken and the wave function is squeezed to the NW surface by a k_z-dependent effective potential. This effect results in a finite SO coupling, which is also sensitive to the geometrical confinement. As we have shown, at low magnetic field (< 1T for the considered NW), when orbital effects are weak, the SO coupling is isotropic with respect to the magnetic field in the NW section. Interestingly, the slight sixfold anisotropy appears at higher magnetic fields (or high electron concentration), when the wave function is squeezed to the NW edges to a larger extent.

When a gate potential is applied in the direction orthogonal to the magnetic field, the two fields intertwine in a way which may enhance or suppress the SO coupling, depending on the relative direction, leading to a twofold anisotropy with respect to the magnetic field rotation in the x-y plane. Our study for the axially magnetic field, relevant to Majorana zero state engineering, shows no significant modification of the SO constant in the magnetic field range used in the Majorana experiments.

Note that the electron-electron interaction, here introduced at the mean-field level, is essential in estimating SO coupling constants, via charge localization. At the high concentration regime total energy is minimized by reducing repulsive Coulomb energy, moving electrons outwards, near to the facets where the electric field becomes the largest. Due to the prismatic symmetry of the NW, charge localizes in six quasi-1D channels at the edges. As we discussed, this localization determines the sensitivity of the electronic system to the gate potential and the magnetic field direction.

Finally, in light of our simulations, we have analyzed qualitatively recent experiments with suspended InAs NWs [30], and good agreement with the experimental data has been found. However, we suggest that an unintended electric field is present in the sample, which would reconcile observations with our predictions.

As a final remark, we note that in real devices a dielectric spacer often separates the gate from the NW, which reduces the SO constant. However, a spacer layer could change the cancellation effect, as it only lowers the internal electric field. Moreover, our calculations are performed for a translationally invariant NW. In principle, in experiments finite size effects or tunneling from the leads and/or interchannel scattering may take place and influence the lead-to-lead transmission, particularly in the coherent transport regime of sufficiently short NWs [40]. Note, however, that such effects are unlikely to depend on the external field direction. On the other hand, when estimating magnetotransport conductance, SOC is a crucial material-related ingredient. Our paper shows how SOC intrinsically depend on the direction of the external field.

ACKNOWLEDGMENTS

This work was supported by the AGH UST statutory tasks No. 11.11.220.01/2 within subsidy of the Ministry of Science and Higher Education in part by PL-Grid Infrastructure.

[1] H. C. Koo, J. H. Kwon, J. Eom, J. Chang, S. H. Han, and M. Johnson, Science **325**, 1515 (2009).
[2] P. Wójcik, J. Adamowski, B. J. Spisak, and M. Wołoszyn, J. Appl. Phys. **115**, 104310 (2014).
[3] P. Wójcik and J. Adamowski, Sci. Rep. **7**, 45346 (2017).
[4] A. T. Ngo, P. Debray, and S. E. Ulloa, Phys. Rev. B **81**, 115328 (2010).
[5] M. Kohda, S. Nakamura, Y. Nishihara, K. Kobayashi, T. Ono, J. O. Ohe, Y. Tokura, T. Mineno, and J. Nitta, Nat. Commun. **3**, 1082 (2012).
[6] S. Nadj-Perge, S. M. Frolov, E. P. A. M. Bakkers, and L. P. Kouwenhoven, Nature (London) **468**, 1084 (2010).
[7] J. W. G. van den Berg, S. Nadj-Perge, V. S. Pribiag, S. R. Plissard, E. P. A. M. Bakkers, S. M. Frolov, and L. P. Kouwenhoven, Phys. Rev. Lett. **110**, 066806 (2013).
[8] J. Kammhuber, M. C. Cassidy, F. Pei, M. P. Nowak, A. Vuik, D. Car, S. R. Plissard, E. P. A. M. Bakkers, M. Wimmer, and L. P. Kouwenhoven, Nat. Commun. **8**, 478 (2017).
[9] S. Heedt, N. Traverso Ziani, F. Crépin, W. Prost, S. Trellenkamp, J. Schubert, D. Grützmacher, B. Trauzettel, and T. Schäpers, Nat. Phys. **13**, 563 (2017).
[10] I. van Weperen, B. Tarasinski, D. Eeltink, V. S. Pribiag, S. R. Plissard, E. P. A. M. Bakkers, L. P. Kouwenhoven, and M. Wimmer, Phys. Rev. B **91**, 201413(R) (2015).
[11] T. Campos, P. E. Faria Junior, M. Gmitra, G. M. Sipahi, and J. Fabian, Phys. Rev. B **97**, 245402 (2018).
[12] P. Wójcik, A. Bertoni, and G. Goldoni, Appl. Phys. Lett. **114**, 073102 (2019).
[13] P. Wójcik, A. Bertoni, and G. Goldoni, Phys. Rev. B **97**, 165401 (2018).
[14] A. Bringer, S. Heedt, and T. Schäpers, Phys. Rev. B **99**, 085437 (2019).
[15] X. W. Zhang and J. B. Xia, Phys. Rev. B **74**, 075304 (2006).
[16] K. Takase, K. Tateno, and S. Sasaki, Appl. Phys. Express **12**, 117002 (2019).
[17] J. Alicea, Rep. Prog. Phys. **75**, 076501 (2012).
[18] A. Kitaev, Ann. Phys. **303**, 2 (2003).
[19] S. Das Sarma, M. Freedman, and C. Nayak, npj Quantum Inf. **1**, 15001 (2015).
[20] Y. Oreg, G. Refael, and F. von Oppen, Phys. Rev. Lett. **105**, 177002 (2010).
[21] K. O. Klausen, A. Sitek, S. I. Erlingsson, and A. Manolescu, Nanotechnology **31**, 354001 (2020).
[22] V. Mourik, K. Zuo, S. M. Frolov, S. R. Plissard, E. P. A. M. Bakkers, and L. P. Kouwenhoven, Science **336**, 1003 (2012).
[23] S. M. Albrecht, A. P. Higginbotham, M. Madsen, F. Kuemmeth, T. S. Jespersen, J. Nygård, P. Krogstrup, and C. M. Marcus, Nature (London) **531**, 206 (2016).
[24] J. D. Sau, S. Tewari, and S. Das Sarma, Phys. Rev. B **85**, 064512 (2012).
[25] G. Dresselhaus, Phys. Rev. **100**, 580 (1955).
[26] E. I. Rashba, Sov. Phys. Solid State **2**, 1109 (1960).
[27] A. Manchon, H. C. Koo, J. Nitta, S. M. Frolov, and R. A. Duine, Nat. Mater. **14**, 871 (2015).
[28] S. Nadj-Perge, V. S. Pribiag, J. W. G. van den Berg, K. Zuo, S. R. Plissard, E. P. A. M. Bakkers, S. M. Frolov, and L. P. Kouwenhoven, Phys. Rev. Lett. **108**, 166801 (2012).
[29] B. D. Woods, S. Das Sarma, and T. D. Stanescu, Phys. Rev. B **99**, 161118 (2019).
[30] A. Iorio, M. Rocci, L. Bours, M. Carrega, V. Zannier, L. Sorba, S. Roddaro, F. Giazotto, and E. Strambini, Nano Lett. **19**, 652 (2019).
[31] J.-W. Luo, L. Zhang, and A. Zunger, Phys. Rev. B **84**, 121303 (2011).
[32] J. Fabian, A. Matos-Abiague, C. Ertler, P. Stano, and I. Žutić, Acta Phys. Slovaca **57**, 565 (2007).

[33] M. P. Nowak and P. Wójcik, Phys. Rev. B **97**, 045419 (2018).
[34] A. Bertoni, M. Royo, F. Mahawish, and G. Goldoni, Phys. Rev. B **84**, 205323 (2011).
[35] M. Royo, A. Bertoni, and G. Goldoni, Phys. Rev. B **89**, 155416 (2014).
[36] I. Vurgaftman, J. R. Meyer, and L. R. Ram-Mohan, Appl. Phys. Lett. **89**, 5815 (2001).
[37] M. Royo, A. Bertoni, and G. Goldoni, Phys. Rev. B **87**, 115316 (2013).
[38] G. W. Winkler, D. Varjas, R. Skolasinski, A. A. Soluyanov, M. Troyer, and M. Wimmer, Phys. Rev. Lett. **119**, 037701 (2017).
[39] M. Royo, C. Segarra, A. Bertoni, G. Goldoni, and J. Planelles, Phys. Rev. B **91**, 115440 (2015).
[40] A. Aharony, O. Entin-Wohlman, M. Jonson, and R. I. Shekhter, Phys. Rev. B **97**, 220404(R) (2018).